International Journal of Solids and Structures 296 (2024) 112815

Contents lists available at ScienceDirect

International Journal of Solids and Structures

journal homepage: www.elsevier.com/locate/ijsolstr

Numerical analyses of brittle crack growth experiments in compression using a modified phase-field theory

P. Hesammokri *, P. Isaksson

Solid Mechanics, The Ångström Laboratory, Uppsala University, SE-751 21, Uppsala, Sweden

ARTICLE INFO

Keywords:
Phase-field fracture theory
Decomposition
Mixed-mode fracture
Compression

ABSTRACT

There has been a huge interest in recent years in using phase-field theories for numerical analyses of fracture phenomena. However, in phase-field fracture theories, a critical aspect often involves a decomposition of the strain energy density to select physically trustworthy crack paths and to prevent interpenetration of crack surfaces. This aspect becomes even more critical in the case of mixed-mode loading under compression. To overcome these challenges, a hydrostatic-spectral-deviatoric decomposition, enhanced by separate critical energy release rates for different fracture modes, is employed in this study. In order to evaluate the enhanced decomposition strategy, a set of biaxially loaded crack experiments in global compression is designed. Samples of different geometries contain multiple flaws and holes. The experiments are numerically simulated using a unified set of material parameters and three different strain energy decomposition methods (i.e., hydrostatic-spectral-deviatoric, spectral and hydrostatic–deviatoric). Simulations using the hydrostatic-spectral-deviatoric decomposition scheme capture both intricate crack paths and critical loads in the experiments. The enhanced decomposition strategy seems capable of simulating the experiments with reasonable precision, in sharp contrast to the two commonly used decomposition strategies (spectral and hydrostatic–deviatoric).

1. Introduction

Understanding and analyzing crack growth in materials is crucial in various scientific areas. In numerical analyses of fracture using finite element methods, two well-known approaches are discrete crack representations and diffuse crack representations. Discrete crack representations involve strong intra-element level displacement discontinuities (Moës and Belytschko, 2002; Armero and Linder, 2009), requiring criteria based on stress, strain, or energy release rates and complex procedures like virtual crack closure and re-meshing techniques. In contrast, diffuse crack approaches, such as continuum damage models and phase-field fracture models (cf. Peerlings et al., 1996; Areias et al., 2016; Miehe et al., 2010b,a; Borden et al., 2012), maintain displacement field continuity. Phase-field fracture models, particularly notable for their application in complex fracture problems without re-meshing, are based on an energy minimization problem coupling strain and fracture energies. Phase-field models can often predict crack nucleation, propagation, merging and branching in brittle materials, finding widespread use in different aspects like dynamic simulations and analyzing heterogeneous materials (cf. Borden et al., 2012; Larsen et al., 2010; Hofacker and Miehe, 2012; Carlsson and Isaksson, 2018, 2019; Schlüter et al., 2016; Kuhn and Müller, 2016; Espadas-Escalante et al., 2019; Espadas-Escalante and Isaksson, 2019).

Phase-field fracture theories are rooted in Griffith's variational principles and was developed by Francfort and Marigo (1998), and later by Bourdin et al. (2000). The theories often involve decomposing the strain energy density into positive (tensile) and negative (compressive) terms. The positive part is assumed to contribute to material stiffness degradation, while the negative part is presumed to have no influence on the degradation process (Ambati et al., 2015). Two well-known methods for decomposing the strain energy density are the hydrostatic–deviatoric decomposition (Amor et al., 2009) and the spectral decomposition (Miehe et al., 2010b). However, these models face limitations in simulating fractures under shear and compressive loading situations (Hesammokri et al., 2023). The spectral decomposition struggles in shear scenarios, where material stiffness may persist with a fully developed crack, while the hydrostatic–deviatoric decomposition faces challenges in mixed-mode compressive loading, leading to complete stiffness loss even upon crack contact.

In the literature, compression-dominated phase-field fractures are mainly applied in rock mechanics. An attempt to modify the spectral decomposition for mixed-mode brittle fractures was proposed by Zhang et al. (2017a), who assumed different critical energy release rates for different crack modes, based on the pioneering work (Shen and Stephansson, 1994). Other similar modifications for mixed-mode

* Corresponding author.
E-mail address: parnian.hesammokri@angstrom.uu.se (P. Hesammokri).

https://doi.org/10.1016/j.ijsolstr.2024.112815
Received 28 November 2023; Received in revised form 2 April 2024; Accepted 4 April 2024
Available online 12 April 2024

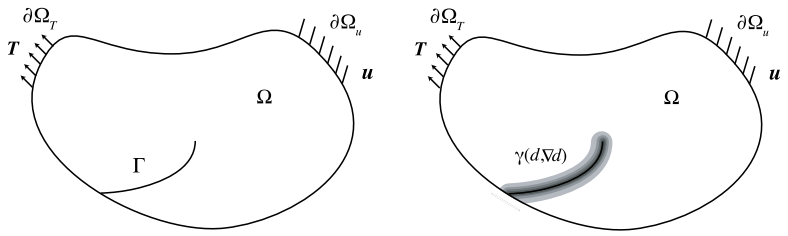

Fig. 1. Discrete vs diffusive crack representation.

fracture have been suggested, cf. Spetz et al. (2020, 2021), Shajan et al. (2023). However, these modifications are not completely satisfactory, mainly because they are based on various spectral decomposition formulations preventing material stiffness degradation even when cracks are fully developed under pure shear load.

To circumvent these issues, a modification was introduced by the authors (Hesammokri et al., 2023). This modified decomposition of strain energy density combines key aspects from both the spectral and the hydrostatic–deviatoric decomposition methods while incorporating a classical Mohr failure criterion. A distinctive feature of this decomposition strategy lies in its potential to assess whether a compressive deformation field effectively contributes to the crack-driving process or not. While the so-called hydrostatic-spectral-deviatoric decomposition (Hesammokri et al., 2023) has exhibited promising results, its capability to accurately replicate diverse crack paths and loading curves in different experimental scenarios remains uncertain and requires further investigation. Moreover, to illustrate the complexity of the problem, a striking observation is made when contrasting experimental findings for brittle specimens containing two inclined flaws subjected to global compression, such as reported in e.g. Bobet and Einstein (1998) and Nguyen (2011). While mode I and mode II cracks were reported to emerge in Bobet and Einstein (1998), mode I and compressive/crushing cracks were observed in Nguyen (2011). Thus, variations in material properties like compressive strength and mode I/II fracture toughness lead to entirely different crack paths under similar remote loading conditions.

In this study, an enhanced version of the hydrostatic-spectral-deviatoric decomposition is implemented in finite element models, featuring distinct critical energy release rates for different fracture modes. The main objective is to assess the model's ability to predict crack paths, which is achieved through a series of experiments in global compression. Specimens are manufactured of gypsum plaster and contain embedded flaws and holes. The numerical results obtained using a unique set of material parameters are compared to the experimental results, considering both crack paths and loading curves. A good agreement between the numerical simulations and experimental observations not only demonstrates the model's accuracy but also highlights its ability to provide valuable mechanistic insights into the complex fracture behavior of brittle materials.

2. Theory

Consider an isotropic linearly-elastic body, denoted as Ω, Fig. 1, which includes an external boundary $\partial\Omega$ and a distinct crack Γ. A part of the boundary $\partial\Omega_{\boldsymbol{T}}$ is subject to traction $\boldsymbol{T}$, while $\partial\Omega_{\boldsymbol{u}}$ is subject to displacement $\boldsymbol{u}$. The total energy of the system can be formulated as

$$\Pi(\boldsymbol{u},d)=\int_{\Omega}\Psi_e\mathrm{d}\Omega+\int_{\Gamma}G_c\mathrm{d}s, \tag{1}$$

where the term Ψ_e represents the strain energy density and G_c represents the critical energy release rate. A damage parameter d is introduced, $0\le d\le 1$, so that a material point is intact when $d=0$ and fully damaged when $d=1$. The last term in (1) accounts for the energy used in creating new surfaces. Further, in a phase-field theory, the discrete crack Γ is approximated using a crack density function $\gamma(d,\nabla d)$, Fig. 1. This functional belongs to a family of elliptic functionals that approximate the Mumford–Shah functional (Braides, 1998). In this study, a crack density functional featuring linearity in d and quadratic dependence on ∇d, known as the AT1 model (Pham et al., 2011), is used. Unlike functionals with quadratic dependence on d (known as the AT2 model) that initiate damage evolution upon the application of load, resulting in the absence of a purely elastic response, the AT1 functional employed in this work maintains an elastic phase in the material until the point of fracture initiation (Suh et al., 2020; Geelen et al., 2019; Wu and Nguyen, 2018). The AT1 functional also promotes a more localized damage zone than the quadratic crack density functional AT2 (Bleyer and Alessi, 2018; Tanné et al., 2018). Using AT1, the second term in (1) is approximated as

$$\int_{\Gamma}G_c\mathrm{d}s\approx G_c\int_{\Omega}\gamma(d,\nabla d)\mathrm{d}\Omega=G_c\int_{\Omega}\frac{3}{8l}(d+l^2\nabla d\cdot\nabla d)\mathrm{d}\Omega, \tag{2}$$

where l is a regularization parameter, controlling the width of the diffuse crack. Furthermore, in order to prevent crack growth in compression, the strain energy density is separated into two components: a positive portion related to tensile strain and a negative portion related to compressive strain. It is assumed that only the positive component has an impact on the damage mechanism (stiffness degradation), cf. Ambati et al. (2015), i.e.,

$$\int_{\Omega}\Psi_e\mathrm{d}\Omega=\int_{\Omega}[(1-d)^2\Psi_e^{+}+\Psi_e^{-}]\mathrm{d}\Omega. \tag{3}$$

The Cauchy stress tensor $\boldsymbol{\sigma}$ and the consistent elastic stiffness tensor $\mathbf{C}$ are given by

$$\boldsymbol{\sigma}=(1-d)^2\frac{\mathrm{d}\Psi_e^{+}}{\mathrm{d}\boldsymbol{\epsilon}}+\frac{\mathrm{d}\Psi_e^{-}}{\mathrm{d}\boldsymbol{\epsilon}},\quad\text{and} \tag{4}$$

$$\mathbf{C}=(1-d)^2\frac{\mathrm{d}^2\Psi_e^{+}}{\mathrm{d}\boldsymbol{\epsilon}^2}+\frac{\mathrm{d}^2\Psi_e^{-}}{\mathrm{d}\boldsymbol{\epsilon}^2}, \tag{5}$$

where $\boldsymbol{\epsilon}=\frac{1}{2}[\nabla\boldsymbol{u}+(\nabla\boldsymbol{u})^T]$ is the linearized strain tensor. Now, using the above relations, the total energy in the body is given by

$$\Pi(\boldsymbol{u},d)=\int_{\Omega}[(1-d)^2\Psi_e^{+}+\Psi_e^{-}+\frac{3G_c}{8l}(d+l^2\nabla d\cdot\nabla d)]\mathrm{d}\Omega. \tag{6}$$

According to e.g. Shen and Stephansson (1994), Nejati et al. (2021) can the critical energy release rates be different for different fracture modes in rock-like materials. Considering a rock specimen containing a single inclined flaw subjected to compression, a distinctive sequence unfolds: primary wing cracks develop followed by secondary cracks (sometimes interpreted as shear, or mode II, cracks). The sequential appearance of the primary and secondary cracks can be attributed to the considerable difference in the critical energy release rates for different crack modes. It has been argued that this phenomenon cannot be captured by using a traditional critical energy release criterion (Shen and Stephansson, 1994). The critical energy release rate for an opening (mode I) crack, $G_{c\mathrm{I}}$, can be significantly smaller than that for a shear (mode II) crack, $G_{c\mathrm{II}}$ (Li, 1986). Zhang et al. (2017a) suggested a separation of the strain energy densities to associate different critical energy release rates involved in mixed-mode I/II crack growth. Other studies delved into defining normal and tangential vectors to tackle mixed-mode I/II fracture (Bryant and Sun, 2018) as well as exploring crack orientation vectors (Steinke et al., 2022). For the sake of

simplicity, we apply the strategy outlined in Zhang et al. (2017a) to handle different mode-dependent fracture toughness in brittle materials subject to mixed-mode loading in compression. The positive strain energy density Ψ_e^+ is decomposed into two parts, i.e.,

$$\Psi_e^+ = \Psi_{\mathrm{I}} + \Psi_{\mathrm{II}}, \tag{7}$$

where Ψ_{I} is associated with mode I fracture and Ψ_{II} is associated with mode II fracture. Introducing $G_{c\mathrm{I}}$ and $G_{c\mathrm{II}}$, the ratio Ψ_e^+/G_c is written as (Zhang et al., 2017a)

$$\frac{\Psi_e^+}{G_c} = \frac{\Psi_{\mathrm{I}}}{G_{c\mathrm{I}}} + \frac{\Psi_{\mathrm{II}}}{G_{c\mathrm{II}}}. \tag{8}$$

Further, to establish irreversible crack growth in computer simulations, a history field $\mathcal{H}$ is defined using (8), i.e.,

$$\mathcal{H}(\boldsymbol{u},t) = \max_{\tau\in[0,t]}\{\frac{\Psi_e^+}{G_c}\} = \max_{\tau\in[0,t]}\{\frac{\Psi_{\mathrm{I}}}{G_{c\mathrm{I}}} + \frac{\Psi_{\mathrm{II}}}{G_{c\mathrm{II}}}\}, \tag{9}$$

where t denotes time. The presence of the history field $\mathcal{H}$ ensures that the highest strain energy density experienced during the loading history of the material determines its current damage state, preventing any possibility of healing (Miehe et al., 2010b). It is important to note that stresses are still reversible and their evaluation follows (4).

Considering the principle of minimizing potential energy, it is expected that the first variation of (6) vanishes. The Euler–Lagrange equations for (6), considering both the displacement and damage fields are,

$$\nabla\cdot\boldsymbol{\sigma} = 0, \quad \text{and} \quad (1-d)\mathcal{H} - \frac{3}{16l} - \frac{3l}{8}\nabla^2 d = 0. \tag{10}$$

2.1. Spectral decomposition

Miehe et al. (2010b) introduced a spectral decomposition that decomposes the strain energy density based on tensile deformation states. In an isotropic linear elastic material, the strain energy density can be expressed in terms of Lamé parameters λ and μ as $\Psi_e = \frac{1}{2}\lambda(\mathrm{tr}\,\boldsymbol{\epsilon})^2 + \mu\,\mathrm{tr}\,(\boldsymbol{\epsilon}^2)$. The first term relates to volumetric deformation, while the second term includes volume and shape changes. Since $\mathrm{tr}\,\boldsymbol{\epsilon}$ and $\mathrm{tr}\,(\boldsymbol{\epsilon}^2)$ are invariants of the strain tensor, they do not change with any rotation of the coordinate system, which allows decomposing of the strain energy density into positive and negative parts using the principal strains. The first step is to express the strain energy density in terms of principal strains ϵ_1, ϵ_2 and ϵ_3 as $\Psi_e = \frac{1}{2}\lambda(\epsilon_1+\epsilon_2+\epsilon_3)^2 + \mu(\epsilon_1^2+\epsilon_2^2+\epsilon_3^2)$. The strain energy density is then separated into positive and negative parts using the strictly positive and negative terms i.e.,

$$\Psi_e^{\pm} = \tfrac{1}{2}\lambda\langle\epsilon_1+\epsilon_2+\epsilon_3\rangle_{\pm}^2 + \mu\langle\epsilon_1\rangle_{\pm}^2 + \mu\langle\epsilon_2\rangle_{\pm}^2 + \mu\langle\epsilon_3\rangle_{\pm}^2, \tag{11}$$

where $\langle\cdot\rangle_+$ and $\langle\cdot\rangle_-$ select the positive and negative parts of their argument, i.e. $\langle x\rangle_+ = x$, if $x \geq 0$; 0 if $x < 0$, and $\langle x\rangle_- = x$, if $x \leq 0$; 0 if $x > 0$. The associated mode I and mode II contributions to the positive strain energy density are assumed as

$$\Psi_{\mathrm{I}} = \tfrac{1}{2}\lambda\langle\epsilon_1+\epsilon_2+\epsilon_3\rangle_+^2, \quad \text{and} \quad \Psi_{\mathrm{II}} = \mu\langle\epsilon_1\rangle_+^2 + \mu\langle\epsilon_2\rangle_+^2 + \mu\langle\epsilon_3\rangle_+^2. \tag{12}$$

2.2. Hydrostatic–deviatoric decomposition

Amor et al. (2009) introduced a hydrostatic–deviatoric decomposition, suggesting that crack growth is driven by both shear and tensile bulk deformation. The strain tensor is decomposed into a hydrostatic and a deviatoric part as $\boldsymbol{\epsilon} = \epsilon_K\mathbf{1} + \mathbf{e}$ where $\mathbf{1}$ is the second-order identity tensor, $\mathbf{e}$ is the deviatoric strain tensor and ϵ_K is the hydrostatic strain $\epsilon_K = \mathrm{tr}\,\boldsymbol{\epsilon}/n$ (n is the number of spatial dimensions). Using the bulk modulus $K = \lambda + 2\mu/n$, the strain energy density can then be written as $\Psi_e = \frac{1}{2}K(\mathrm{tr}\,\boldsymbol{\epsilon})^2 + \mu\,\mathrm{tr}\,(\mathbf{e}^2)$ and decomposed into positive and negative parts as

$$\Psi_e^+ = \tfrac{1}{2}K\langle\mathrm{tr}\,\boldsymbol{\epsilon}\rangle_+^2 + \mu\,\mathrm{tr}\,(\mathbf{e}^2), \quad \text{and} \quad \Psi_e^- = \tfrac{1}{2}K\langle\mathrm{tr}\,\boldsymbol{\epsilon}\rangle_-^2. \tag{13}$$

The associated mode I and mode II contributions to the positive strain energy density are assumed as

$$\Psi_{\mathrm{I}} = \tfrac{1}{2}K\langle\mathrm{tr}\,\boldsymbol{\epsilon}\rangle_+^2, \quad \text{and} \quad \Psi_{\mathrm{II}} = \mu\,\mathrm{tr}\,(\mathbf{e}^2). \tag{14}$$

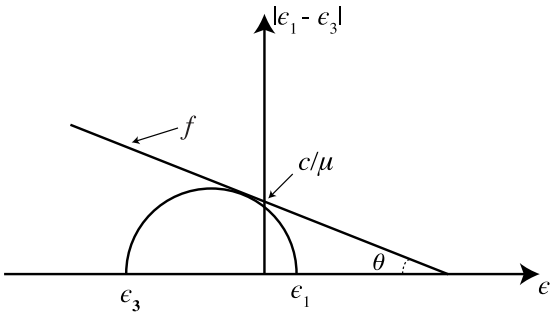

Fig. 2. Mohr diagram and failure envelope.

2.3. Hydrostatic-spectral-deviatoric decomposition

The hydrostatic-spectral-deviatoric decomposition (Hesammokri et al., 2023) can be seen as an interpolation between the spectral and the hydrostatic–deviatoric decompositions. The deviatoric contribution to the strain energy density in the hydrostatic–deviatoric decomposition, denoted as $\Psi_{\mathrm{dev}} = \mu\,\mathrm{tr}\,(\mathbf{e}^2)$, can be written in terms of principal strains as $\Psi_{\mathrm{dev}} = \mu\frac{n-1}{n}(\epsilon_1^2+\epsilon_2^2+\epsilon_3^2) - \mu\frac{2}{n}(\epsilon_1\epsilon_2+\epsilon_1\epsilon_3+\epsilon_2\epsilon_3)$. By employing a spectral decomposition, the deviatoric energy is further decomposed into positive and negative parts as

$$\begin{aligned}\Psi_{\mathrm{dev}}^+ &= \mu\tfrac{n-1}{n}[\langle\epsilon_1\rangle_+^2 + \langle\epsilon_2\rangle_+^2 + \langle\epsilon_3\rangle_+^2] - \mu\tfrac{2}{n}[\langle\epsilon_1\rangle_+\langle\epsilon_2\rangle_- + \langle\epsilon_2\rangle_+\langle\epsilon_1\rangle_- + \\ &\quad \langle\epsilon_1\rangle_+\langle\epsilon_3\rangle_- + \langle\epsilon_3\rangle_+\langle\epsilon_1\rangle_- + \langle\epsilon_3\rangle_+\langle\epsilon_2\rangle_- + \langle\epsilon_2\rangle_+\langle\epsilon_3\rangle_-], \quad \text{and,} \\ \Psi_{\mathrm{dev}}^- &= \mu\tfrac{n-1}{n}[\langle\epsilon_1\rangle_-^2 + \langle\epsilon_2\rangle_-^2 + \langle\epsilon_3\rangle_-^2].\end{aligned} \tag{15}$$

The final formulations for the hydrostatic-spectral-deviatoric decomposition are

$$\Psi_e^+ = \tfrac{1}{2}K\langle\mathrm{tr}\,\boldsymbol{\epsilon}\rangle_+^2 + \Psi_{\mathrm{dev}}^+ + \phi\Psi_{\mathrm{dev}}^-, \quad \text{and} \quad \Psi_e^- = \tfrac{1}{2}K\langle\mathrm{tr}\,\boldsymbol{\epsilon}\rangle_-^2 + (1-\phi)\Psi_{\mathrm{dev}}^-, \tag{16}$$

where ϕ is a variable that can take the value 0 or 1, and controls whether or not Ψ_{dev}^- contributes to crack growth. A classical Mohr failure criterion (Labuz and Zang, 2012) is used to assess whether fracture occurs under compressive loads, i.e., to determine the value of ϕ. The criterion is based on a fracture surface defined as (sorting $\epsilon_1 \geq \epsilon_2 \geq \epsilon_3$)

$$f = \frac{\lambda+\mu}{\mu}\frac{\epsilon_1+\epsilon_3}{\epsilon_1-\epsilon_3}\sin\theta - \frac{c}{\mu(\epsilon_1-\epsilon_3)}\cos\theta + 1\,. \tag{17}$$

In (16), $\phi = 1$ if $f \geq 0$, otherwise $\phi = 0$. The variable c represents an inherent cohesive stress, while θ represents an angle of internal friction as depicted in Fig. 2. The associated mode I and mode II contributions to the positive strain energy density are assumed as

$$\Psi_{\mathrm{I}} = \tfrac{1}{2}K\langle\mathrm{tr}\,\boldsymbol{\epsilon}\rangle_+^2, \quad \text{and} \quad \Psi_{\mathrm{II}} = \Psi_{\mathrm{dev}}^+ + \phi\Psi_{\mathrm{dev}}^-. \tag{18}$$

3. Experiments

In order to validate the three strain energy density decompositions, four different global uniaxial compression tests were designed. Schematics of sample geometries and their loading conditions are shown in Fig. 3. The designed geometries include multiple embedded flaws and holes. The geometries are: a geometry with an inclined notch, a geometry with a single hole, a geometry with an inclined notch and one hole, and a geometry with an inclined notch and two holes (Fig. 3). The dimensions are: $L = 50$ mm, $a = 20$ mm, $b = 15$ mm, $c = 10$ mm, and $\alpha = 45°$. The experimental samples were manufactured of a mixture

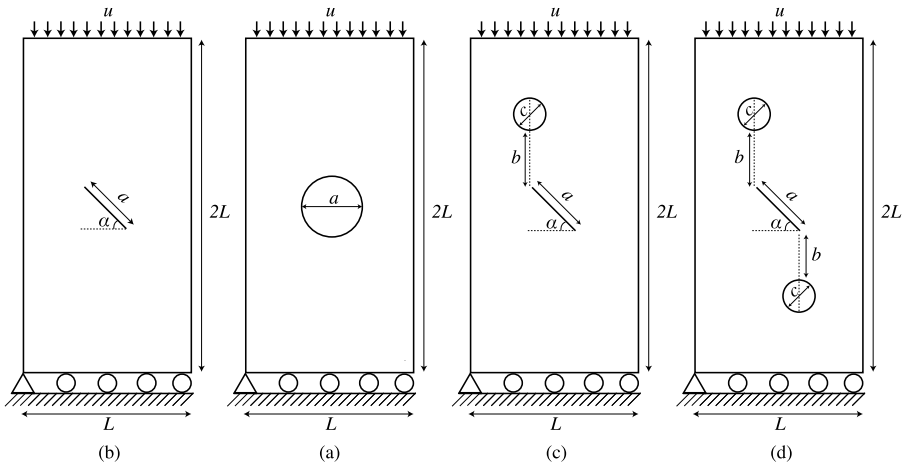

Fig. 3. Load and geometries: Inclined notch (a), single-hole (b), inclined notch with a hole (c), and inclined notch with two holes (d).

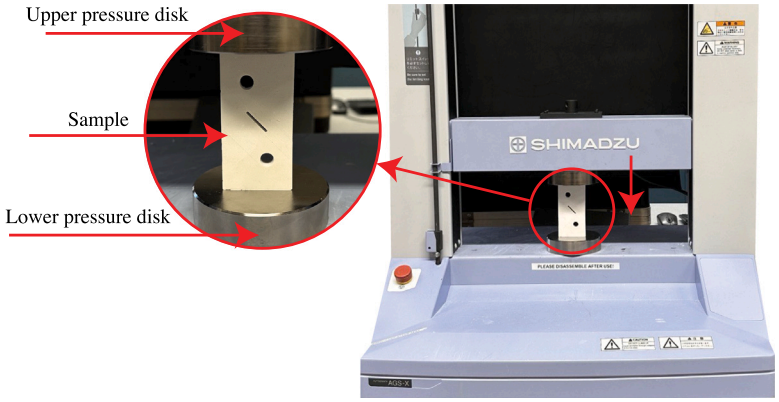

Fig. 4. Experimental set-up with a Shimadzu testing machine.

Table 1
Measured thicknesses for the experimental samples.

Thickness (mm)				
	single-hole	Inclined notch	Inclined notch with one hole	Inclined notch with two holes
Sample 1	6.4	8.5	8.5	9.8
Sample 2	7.1	8.55	9.8	9.1
Sample 3	7.5	8.1	9.6	9.9
Sample 4	7.7	9.7	9.7	9
Simulation	7.2	8.7	9.4	9.5

of gypsum plaster and water which were molded. All batches were mixed using the same proportions of gypsum plaster and water (for our particular gypsum, this equated to a precise combination of two parts gypsum plaster to one part water by mass). The samples were taken out from the molds after three hours and baked in an oven for 90 min in 180°C in order to make them dry and brittle. The thickness for each sample is presented in Table 1. The samples were tested using pressure disks in a testing machine (Fig. 4).

4. Numerical simulations

Numerical simulations were carried out for each of the above-mentioned experiments. The lower horizontal boundaries of the specimens were constrained while the upper horizontal boundaries were subject to a vertical displacement, Fig. 3. The vertical boundaries were held stress-free. All the numerical simulations were done using a unified set of material parameters. Most of the material parameters were estimated from the obtained experimental curves including Young's modulus $E = 650$ MPa, a cohesive strength $c = 21$ MPa, a critical energy release rate for mode I, $G_{cI} = 9.1$ N/m, a critical energy release rate for mode II, $G_{cII} = 130$ N/m, and an internal friction angle $\theta = \pi/6$, which is within common range for rocks according to Wines and Lilly (2003). The ratio between the estimated G_{cI} and G_{cII} is reasonable for rocks and rock-like materials (Spetz et al., 2021). Based on (Gercek, 2007), the Poisson's ratio range for rock-like materials is $0.15 \leq \nu \leq 0.35$, and $\nu = 0.2$ is selected. In each numerical simulation, the applied thickness corresponds to the average measured thickness of the experimental samples, as detailed in Table 1. Moreover, in phase-field finite element fracture models, maintaining a proper ratio between the maximum element edge length h and the regularization length l is crucial for numerical stability and accuracy. The condition $l/h \geq 2$ is often imposed as a practical guideline to strike a balance between these considerations (Zhang et al., 2017b). A smaller ratio of l/h than the lower limit may result in insufficient refinement of the mesh, leading to inaccuracies in capturing the transition zone between intact and fractured regions, and may also introduce numerical instabilities. The specific choice $l/h = 2$ aims to ensure that the mesh is adequately refined without unnecessary computational costs. The employed meshes in the simulations were nearly uniform with a maximum element edge length $h = 252$ μm, wherefore a regularization length $l = 2h = 504$ μm was applied.

All the quasi-static simulations employed a staggered Newton–Raphson scheme. In each load step, the displacement field $\boldsymbol{u}$ and damage field d were solved and updated sequentially through an

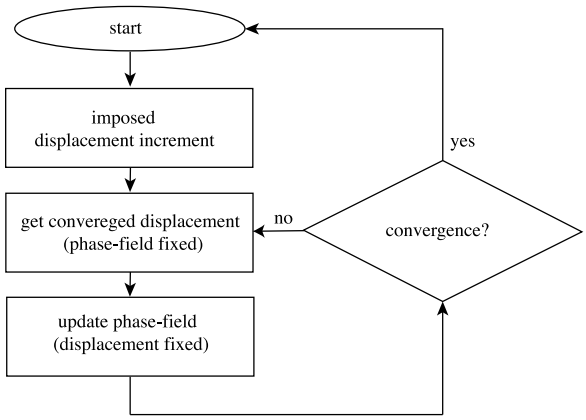

Fig. 5. Flowchart of the staggered scheme used in the quasi-static simulations.

iterative process. This process continued until the incremental changes in displacement and damage reached small enough values and force equilibrium was established. Convergence in the displacement problem was determined using a classical out-of-balance force criterion (Bathe, 1996) (tolerance 10^{-6}). For the damage problem, convergence was considered achieved when the maximum incremental nodal damage field (absolute value) was less than 10^{-3}. It should be mentioned that the initiation of crack growth, or degradation, is exclusively governed by the interplay between energy decomposition and critical energy release rates and the degradation process commences wherever the available energy proves sufficient. A flowchart illustrating the adopted staggered scheme is provided in Fig. 5 to visually represent the process.

The discretization process involves using standard finite element shape functions to approximate the displacement and phase-field variables, cf. Espadas-Escalante et al. (2019). All equations were solved using established finite element algorithms implemented in a Matlab (MATLAB, 2021) code. In the computations, standard bi-linear 4-node isoparametric elements were employed, assuming plane strain conditions. The Lamé coefficients are given by: $\mu = E/[2(1+\nu)]$ and $\lambda = E\nu/[(1+\nu)(1-2\nu)]$. Small deformation theory was assumed and the displacement loads were applied gradually in very small increments. The imposed incremental vertical displacement was 2 μm. All simulations were terminated either when global stiffness loss was achieved or when a crack had grown sufficiently close to a boundary (2/3 of the distance between an initial tip and the boundary).

5. Results and discussion

Global compression experiments were performed for all the sample geometries. The resulting stress–strain relations ($\hat{\sigma}$ is the global stress and $\hat{e}$ is the global strain), as well as the crack paths, for each case, are shown in Figs. 8, 6, 10 and 11. For all three decomposition strategies (spectral, hydrostatic–deviatoric and hydrostatic-spectral-deviatoric), numerical simulations were conducted and the global stress–strain relations and the crack paths were compared to the experimental outcomes.

5.1. Inclined notch

In the inclined notch experiments, primary cracks initiated and grew symmetrically at both sides of the notch's initial tips. Subsequently, secondary cracks gradually propagated horizontally from these tips (see Fig. 6b). Using the hydrostatic-spectral-deviatoric decomposition, the progression of both primary and secondary cracks is effectively depicted (Fig. 6a). There exists a commendable alignment between the global stiffness and experimental observations, as illustrated in Fig. 6c. Fig. 7 shows distributions of the first principal strain ϵ_1, the volumetric strain ϵ_v and the principal shear strain γ, immediately after the onset of the secondary cracks from the notch's initial tips when using the hydrostatic-spectral-deviatoric decomposition. An analysis of the strain fields reveals that the primary cracks predominantly evolve under tension while the secondary cracks grow under compression, implying crushing. Notably, the secondary cracks are driven principally by deviatoric strains, dictated by the Mohr criterion (17). Thus, when the compressive strains reach a critical level, all deviatoric strains contribute to the crack driving positive part of strain energy density Ψ_e^+(16).

It is worth noting that the experimental findings (Fig. 6) in the inclined notch tests closely resemble those reported in Nguyen (2011). The hydrostatic–deviatoric decomposition produces crack paths similar to those obtained using the hydrostatic-spectral-deviatoric decomposition, however, the global stiffness vanishes immediately after the initiation of the secondary cracks (Fig. 6c). Using the spectral decomposition, only the primary cracks developed with no loss in global stiffness.

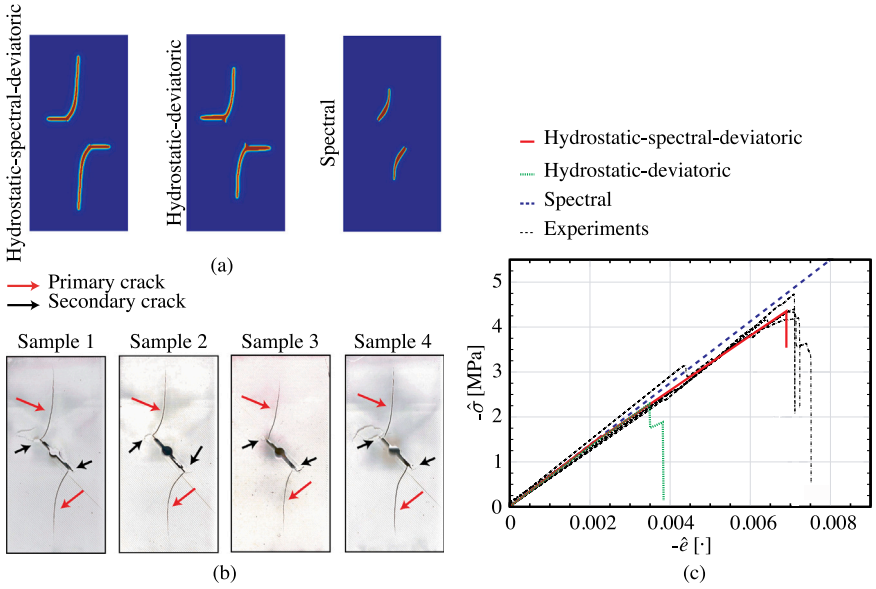

Fig. 6. Inclined notch test: Crack paths for the hydrostatic-spectral-deviatoric, hydrostatic–deviatoric, spectral decomposition models (a), and for the experimental samples (b). Global stress–strain curves (c).

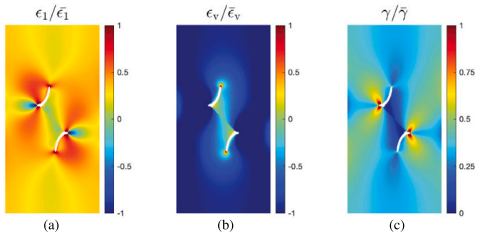

Fig. 7. Inclined notch simulation: Distributions of first principal strain ϵ_1 (a), volumetric strain ϵ_v (b), and principal shear strain γ (c), using the hydrostatic-spectral-deviatoric decomposition. The strain fields are normalized by their highest values, $\bar{\epsilon}_1$, $\bar{\epsilon}_v$ and $\bar{\gamma}$, respectively.

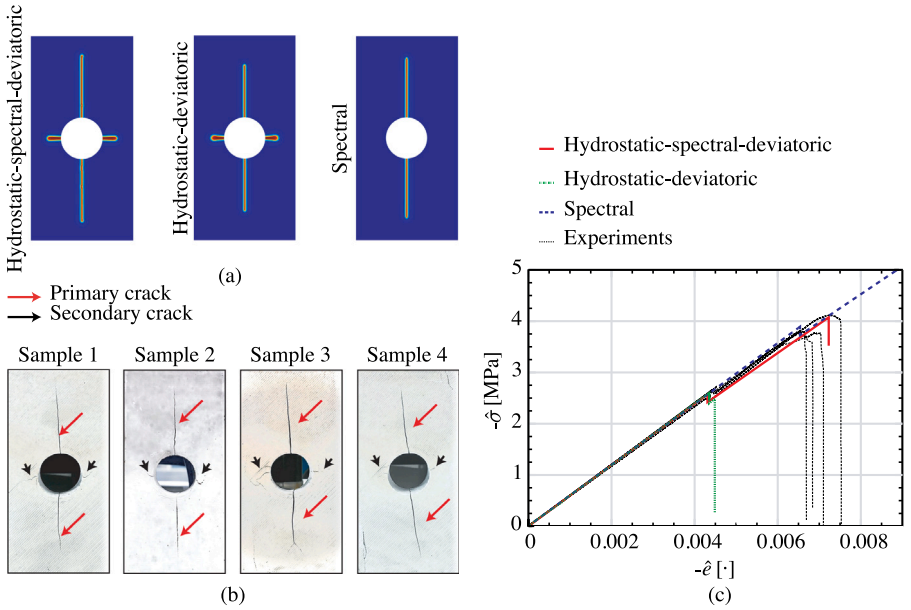

Fig. 8. Single-hole test: Crack paths for the hydrostatic-spectral-deviatoric, hydrostatic–deviatoric, spectral decomposition models (a), and for the experimental samples (b). Global stress–strain curves (c).

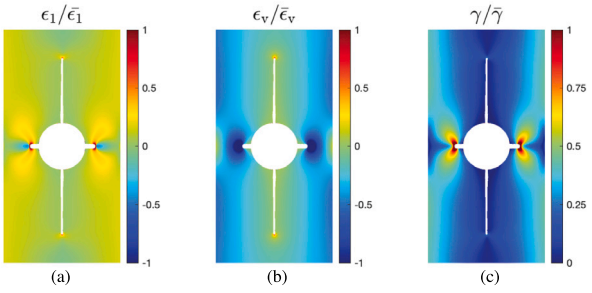

Fig. 9. Single-hole simulation:Distributions of first principal strain ϵ_1 (a), volumetric strain ϵ_v (b), and principal shear strain γ (c), using the hydrostatic-spectral-deviatoric decomposition. The strain fields are normalized by their highest values, $\bar{\epsilon}_1$, $\bar{\epsilon}_v$ and $\bar{\gamma}$, respectively.

5.2. Single-hole

In the single-hole experiments, primary cracks developed vertically along the hole's upper and lower edges followed by two secondary cracks that gently propagated along the far left and far right sides of the hole (Fig. 8). In the numerical simulation using the hydrostatic-spectral-deviatoric decomposition, the same sequence is observed. The first drop in the global stiffness marks the onset of the primary cracks, aligning with experimental observations (Fig. 8c). The subsequent sharp drop in global stiffness represents the emergence of secondary cracks. When analyzing the strain distributions in Fig. 9, a pattern closely resembling that of the previous case is noted. The primary cracks grow under tension while the secondary cracks predominantly grow under compression, driven by deviatoric strains dictated by the Mohr criterion (17).

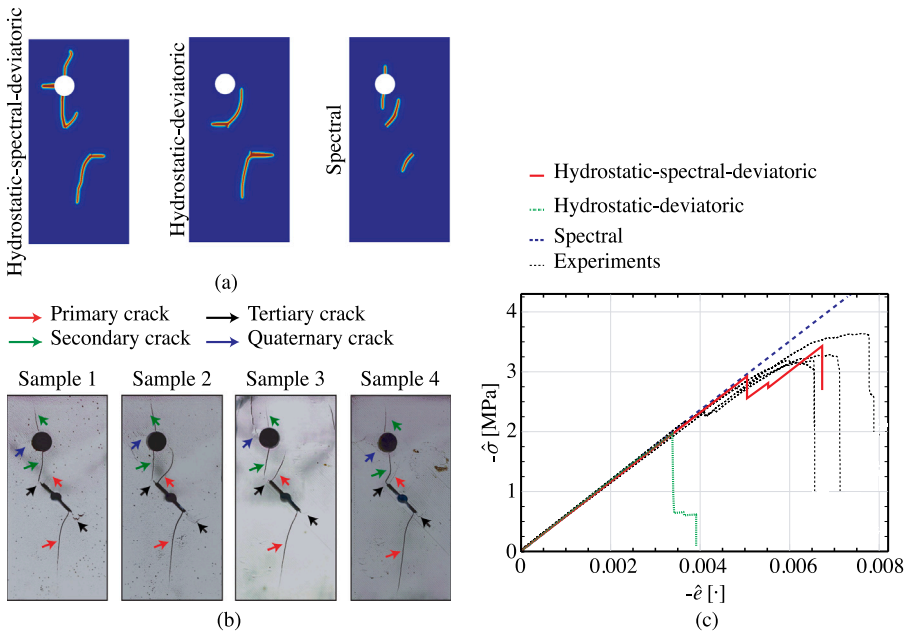

Fig. 10. Inclined notch with one hole: Crack paths for the hydrostatic-spectral-deviatoric, hydrostatic–deviatoric, spectral decomposition models (a), and for the experimental samples (b). Global stress–strain curves (c).

The hydrostatic–deviatoric decomposition results in crack paths similar to those obtained through the hydrostatic-spectral-deviatoric decomposition, however, as in the previous case, the global stiffness vanishes immediately after initiation of the secondary cracks (Fig. 8c). In the spectral decomposition, only primary cracks are observed, indicated by a minor global stiffness decrease. After the onset of the primary cracks, the global stiffness remains unaffected.

5.3. Inclined notch with one hole

In the experiments with one hole and an inclined notch (non-symmetrical case), a distinct sequence of cracks developed, as indicated in Fig. 10. Initially, mirroring the behavior observed in the inclined notch test, we observed the formation of primary cracks at the notch's initial tips. Subsequently, a set of secondary cracks emerged at the upper and lower edges of the hole. Following this phase, small cracks (tertiary cracks) began to grow horizontally from the notch's initial tips. The tertiary crack at the left tip eventually merged with the lower secondary crack. Later in the process, another crack (quaternary crack) was initiated from the far-left edge of the hole. Remarkably, all these cracks, including their merging, are well captured and simulated using the hydrostatic-spectral-deviatoric decomposition (Fig. 10a). Notably, the global stress–strain relationship obtained from both experiments and numerical simulation exhibits a reasonable level of agreement, as depicted in Fig. 10c. Drawing from the earlier discussion and the strain distributions depicted in Figs. 7 and 9, it becomes apparent that the primary and the secondary cracks are in this test mainly growing under tension, while the tertiary and the quaternary cracks are primarily growing under compression, driven by deviatoric strains dictated by the Mohr criterion. Using the hydrostatic–deviatoric decomposition, only the primary and the tertiary cracks were obtained. The global stiffness vanishes after the onset of the horizontal tertiary cracks and this phenomenon hinders the progression of subsequent crack formations. Using the spectral decomposition, only primary and secondary cracks are developed, accompanied by an insignificant loss in global stiffness, an observation consistent with the patterns in the two preceding cases.

5.4. Inclined notch with two holes

In the experiments featuring two holes and an inclined notch, similar to the previous scenarios, a distinct sequence of cracks occurred (Fig. 11). Initially, primary cracks formed at the notch's initial tips, followed by secondary cracks at the upper and lower edges of the holes. Then, small cracks (tertiary cracks) began to propagate horizontally from the notch's initial tips, eventually merging with the developed secondary cracks. Later, additional cracks started to grow from the far-left and far-right edges of the holes (quaternary cracks). Remarkably, employing the hydrostatic-spectral-deviatoric decomposition, the simulation captures all these crack phenomena (Fig. 11a). The global stress–strain curves in the experiments and the numerical simulation exhibit a reasonable level of agreement, Fig. 11c. Similarly to the discussions above, the primary and the secondary cracks are here growing in tension, whereas the tertiary and the quaternary cracks have grown under compression, driven by deviatoric strains dictated by the Mohr criterion. Using the hydrostatic–deviatoric decomposition, only the primary and the tertiary cracks developed and the global stiffness vanished immediately after initiation of the horizontal cracks. When using the spectral decomposition, like in the previous scenarios, only the primary and the secondary cracks developed while the global stiffness was kept.

5.5. Discussion

Based on the presented results, it is apparent that the hydrostatic-spectral-deviatoric decomposition exhibits a potential to replicate crack paths, the sequence of several evolving cracks and the global stress–strain relations with a unified set of material parameters, in sharp contrast to the outcomes when using the hydrostatic–deviatoric or the spectral decompositions. Nevertheless, there might be some minor differences between what is observed in the experiments and what the simulations show in terms of crack paths and the overall stress–strain curves. This is expected and can be attributed to the assumption of a homogeneous material description in the numerical simulations, whereas the experimental material is a hand-made material with inherent complexity. It is worth mentioning that the energy decomposition alone can

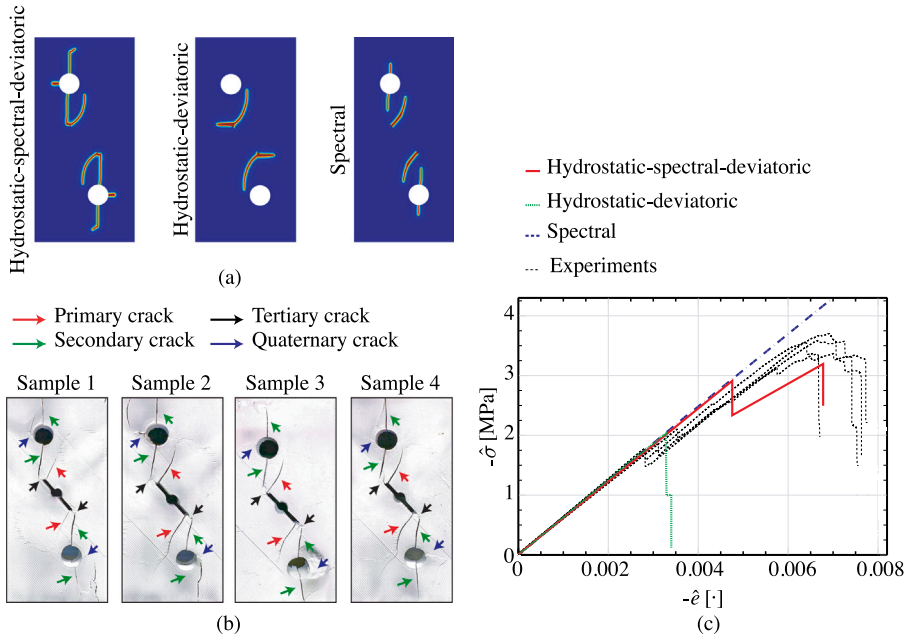

Fig. 11. Inclined notch with two holes: Crack paths for the hydrostatic-spectral-deviatoric, hydrostatic–deviatoric, spectral decomposition models (a), and for the experimental samples (b). Global stress–strain curves (c).

be generalized to both anisotropic and orthotropic formulations, see e.g. van Dijk et al. (2020), and also for material non-linearity. However, incorporating a Mohr failure criterion in an anisotropic formulation is a somewhat trickier endeavor that remains an open scientific question. Moreover, the hydrostatic-spectral-deviatoric decomposition can possibly be further extended, if needed, by e.g. including crack orientation vectors as suggested by Steinke et al. (2022). It is also worth noting that in all simulations performed in this study, the sizes of pre-existing defects (holes and notches) are substantially larger than the utilized regularization length, i.e., the initial defects are able to nucleate localized damage, as explored in e.g. Carlsson and Isaksson (2019, 2020). Finally, it should be mentioned that selecting a Poisson's ratio $\nu = 0.2$ was justified by evaluating simulations using different Poisson's ratio values, as illustrated in Fig. A.1. The outcomes underscore a negligible impact of Poisson's ratio on crack paths and global stress–strain curves.

6. Conclusions

Decomposing the strain energy density into crack driving and crack closure terms is important for preventing crack lips from overlapping and for determining reliable crack paths in numerical simulations using a phase-field theory. However, one challenging aspect when using phase-field methods is in mixed-mode loading conditions where crack growth may occur even under compressive loads. Three different decomposition strategies (spectral, hydrostatic–deviatoric and hydrostatic-spectral-deviatoric) were employed in this study, modified using different critical energy release rates for different fracture modes. A set of biaxially loaded experiments in global compression were performed to examine the validity of the modified models. The experimental samples were manufactured of gypsum plaster and contained flaws and holes.

All experiments were simulated using a unified set of material parameters. Simulated crack paths and global stress–strain relations were compared to the experiments. Simulations employing the spectral decomposition encountered severe difficulties in reproducing crack paths as well as an issue involving never-vanishing global stiffness. While the hydrostatic–deviatoric decomposition reproduced correct crack paths in the simpler experimental cases, it faltered for the more complicated scenarios. In strong contrast, simulations using the hydrostatic-spectral-deviatoric decomposition adeptly replicated the experimental outcomes: intricate crack paths were replicated as well as the global stress–strain curves. In the more complicated experiments; primary, secondary, tertiary and quaternary cracks developed. Using the hydrostatic-spectral-deviatoric decomposition, all those cracks and their paths were captured in the correct order of appearance. Consequently, the enhanced decomposition strategy offers insights into fracture processes in brittle materials subject to mixed-mode loading under compression and seems capable of simulating experimental conditions with reasonable precision.

CRediT authorship contribution statement

P. Hesammokri: Writing – review & editing, Writing – original draft, Visualization, Validation, Software, Formal analysis, Data curation, Conceptualization. **P. Isaksson:** Writing – review & editing, Validation, Supervision, Software, Resources, Project administration, Methodology, Funding acquisition, Formal analysis, Conceptualization.

Declaration of competing interest

The authors declare that they have no known competing financial interests or personal relationships that could have appeared to influence the work reported in this paper.

Data availability

Data will be made available on request.

Appendix. Effect of Poisson's ratio variation

Considering the inclined notch test, the influence of Poisson's ratio variations on the crack paths and global stress–strain curves for the hydrostatic-spectral-deviatoric decomposition is demonstrated in Fig. A.1.

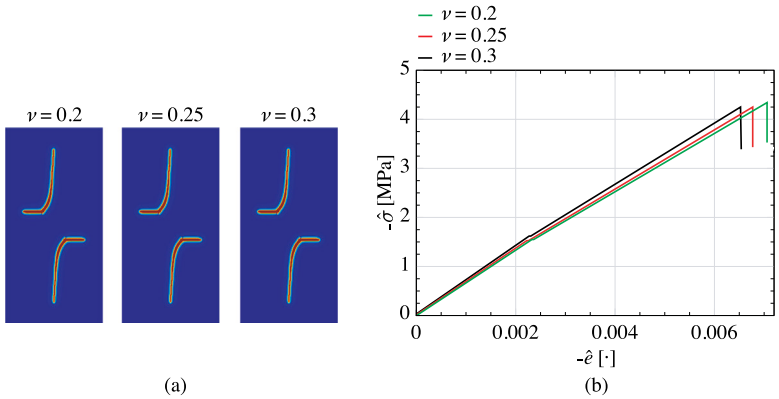

Fig. A.1. The effect of variations in Poisson's ratio on the crack paths (a) and the loading curves (b).

References

Ambati, M., Gerasimov, T., De Lorenzis, L., 2015. A review on phase-field models of brittle fracture and a new fast hybrid formulation. Comput. Mech. 55 (2), 383–405.

Amor, H., Marigo, J.-J., Maurini, C., 2009. Regularized formulation of the variational brittle fracture with unilateral contact: Numerical experiments. J. Mech. Phys. Solid 57 (8), 1209–1229.

Areias, P., Msekh, M., Rabczuk, T., 2016. Damage and fracture algorithm using the screened Poisson equation and local remeshing. Eng. Fract. Mech. 158, 116–143.

Armero, F., Linder, C., 2009. Numerical simulation of dynamic fracture using finite elements with embedded discontinuities. Int. J. Fract. 160 (2), 119–141.

Bathe, K.-J., 1996. Finite Element Procedures. Prentice-Hall.

Bleyer, J., Alessi, R., 2018. Phase-field modeling of anisotropic brittle fracture including several damage mechanisms. Comput. Methods Appl. Mech. Engrg. 336, 213–236.

Bobet, A., Einstein, H., 1998. Fracture coalescence in rock-type materials under uniaxial and biaxial compression. Int. J. Rock Mech. Min. Sci. 35 (7), 863–888.

Borden, M.J., Verhoosel, C.V., Scott, M.A., Hughes, T.J., Landis, C.M., 2012. A phase-field description of dynamic brittle fracture. Comput. Methods Appl. Mech. Eng. 217, 77–95.

Bourdin, B., Francfort, G.A., Marigo, J.-J., 2000. Numerical experiments in revisited brittle fracture. J. Mech. Phys. Solid 48 (4), 797–826.

Braides, A., 1998. Approximation of Free-Discontinuity Problems. Springer.

Bryant, E.C., Sun, W., 2018. A mixed-mode phase-field fracture model in anisotropic rocks with consistent kinematics. Comput. Methods Appl. Mech. Engrg. 342, 561–584.

Carlsson, J., Isaksson, P., 2018. Dynamic crack propagation in wood fibre composites analysed by high speed photography and a dynamic phase field model. Int. J. Solids Struct. 144, 78–85.

Carlsson, J., Isaksson, P., 2019. Crack dynamics and crack tip shielding in a material containing pores analysed by a phase field method. Eng. Fract. Mech. 206, 526–540.

Carlsson, J., Isaksson, P., 2020. A statistical geometry approach to length scales in phase field modelling of fracture and strength of porous microstructures. Int. J. Solids Struct. 200, 83–93.

Espadas-Escalante, J.J., van Dijk, N.P., Isaksson, P., 2019. A phase-field model for strength and fracture analyses of fiber-reinforced composites. Compos. Sci. Technol. 174, 58–67.

Espadas-Escalante, J.J., Isaksson, P., 2019. Mesoscale analysis of the transverse cracking kinetics in woven composite laminates using a phase-field fracture theory. Eng. Fract. Mech. 216, 106523.

Francfort, G.A., Marigo, J.-J., 1998. Revisiting brittle fracture as an energy minimization problem. J. Mech. Phys. Solid 46 (8), 1319–1342.

Geelen, R.J., Liu, Y., Hu, T., Tupek, M.R., Dolbow, J.E., 2019. A phase-field formulation for dynamic cohesive fracture. Comput. Methods Appl. Mech. Engrg. 348, 680–711.

Gercek, H., 2007. Poisson's ratio values for rocks. Int. J. Rock Mech. Min. Sci. 44 (1), 1–13.

Hesammokri, P., Yu, H., Isaksson, P., 2023. An extended hydrostatic–deviatoric strain energy density decomposition for phase-field fracture theories. Int. J. Solids Struct. 262, 112080.

Hofacker, M., Miehe, C., 2012. Continuum phase field modeling of dynamic fracture: variational principles and staggered FE implementation. Int. J. Fract. 178 (1), 113–129.

Kuhn, C., Müller, R., 2016. A discussion of fracture mechanisms in heterogeneous materials by means of configurational forces in a phase field fracture model. Comput. Methods Appl. Mech. Eng. 312, 95–116.

Labuz, J.F., Zang, A., 2012. Mohr–Coulomb failure criterion. Rock Mech. Rock Eng. 45 (6), 975–979.

Larsen, C.J., Ortner, C., Süli, E., 2010. Existence of solutions to a regularized model of dynamic fracture. Math. Models Methods Appl. Sci. 20 (07), 1021–1048.

Li, V.C., 1986. Mechanics of Shear Rupture Applied to Earthquake Zones. Tech. rep..

MATLAB, 2021. R2021b. The MathWorks Inc., Natick, Massachusetts.

Miehe, C., Hofacker, M., Welschinger, F., 2010a. A phase field model for rate-independent crack propagation: Robust algorithmic implementation based on operator splits. Comput. Methods Appl. Mech. Eng. 199 (45–48), 2765–2778.

Miehe, C., Welschinger, F., Hofacker, M., 2010b. Thermodynamically consistent phase-field models of fracture: Variational principles and multi-field FE implementations. Internat. J. Numer. Methods Engrg. 83 (10), 1273–1311.

Moës, N., Belytschko, T., 2002. Extended finite element method for cohesive crack growth. Eng. Fract. Mech. 69 (7), 813–833.

Nejati, M., Bahrami, B., Ayatollahi, M.R., Driesner, T., 2021. On the anisotropy of shear fracture toughness in rocks. Theor. Appl. Fract. Mech. 113, 102946.

Nguyen, T.L., 2011. Endommagement Localisé Dans Les Roches Tendres. Expérimentation Par Mesure De Champs (Ph.D. thesis). Grenoble.

Peerlings, R., Borst, R., Brekelmans, W., Vree, J., Spee, I., 1996. Some observations on localization in non-local and gradient damage models. Eur. J. Mech. A Solids 15 (6), 937–953.

Pham, K., Amor, H., Marigo, J.-J., Maurini, C., 2011. Gradient damage models and their use to approximate brittle fracture. Int. J. Damage Mech. 20 (4), 618–652.

Schlüter, A., Kuhn, C., Müller, R., Gross, D., 2016. An investigation of intersonic fracture using a phase field model. Arch. Appl. Mech. 86 (1), 321–333.

Shajan, A.M., Piska, R., Natarajan, S., 2023. Study of mixed-mode fracture in functionally graded material using an adaptive phase-field fracture model. Compos. Struct. 117708.

Shen, B., Stephansson, O., 1994. Modification of the G-criterion for crack propagation subjected to compression. Eng. Fract. Mech. 177–189.

Spetz, A., Denzer, R., Tudisco, E., Dahlblom, O., 2020. Phase-field fracture modelling of crack nucleation and propagation in porous rock. Int. J. Fract. 224 (1), 31–46.

Spetz, A., Denzer, R., Tudisco, E., Dahlblom, O., 2021. A modified phase-field fracture model for simulation of mixed mode brittle fractures and compressive cracks in porous rock. Rock Mech. Rock Eng. 54 (10), 5375–5388.

Steinke, C., Storm, J., Kaliske, M., 2022. Energetically motivated crack orientation vector for phase-field fracture with a directional split. Int. J. Fract. 237 (1–2), 15–46.

Suh, H.S., Sun, W., O'Connor, D.T., 2020. A phase field model for cohesive fracture in micropolar continua. Comput. Methods Appl. Mech. Engrg. 369, 113181.

Tanné, E., Li, T., Bourdin, B., Marigo, J.-J., Maurini, C., 2018. Crack nucleation in variational phase-field models of brittle fracture. J. Mech. Phys. Solids 110, 80–99.

van Dijk, N.P., Espadas-Escalante, J.J., Isaksson, P., 2020. Strain energy density decompositions in phase-field fracture theories for orthotropy and anisotropy. Int. J. Solids Struct. 196, 140–153.

Wines, D., Lilly, P., 2003. Estimates of rock joint shear strength in part of the Fimiston open pit operation in Western Australia. Int. J. Rock Mech. Min. Sci. 40 (6), 929–937.

Wu, J.-Y., Nguyen, V.P., 2018. A length scale insensitive phase-field damage model for brittle fracture. J. Mech. Phys. Solids 119, 20–42.

Zhang, X., Sloan, S.W., Vignes, C., Sheng, D., 2017a. A modification of the phase-field model for mixed mode crack propagation in rock-like materials. Comput. Methods Appl. Mech. Eng. 322, 123–136.

Zhang, X., Vignes, C., Sloan, S.W., Sheng, D., 2017b. Numerical evaluation of the phase-field model for brittle fracture with emphasis on the length scale. Comput. Mech. 59, 737–752.